Check for updates

Sea-level stability over geological time owing to limited deep subduction of hydrated mantle

N. G. Cerpa [1] ✉, D. Arcay [1] and J. A. Padrón-Navarta [1,2]

Liquid surface oceans are a seemingly unique feature of Earth. Long-term, global sea level depends on the balance of water fluxes between Earth's mantle and surface: between mantle degassing through volcanism and mantle regassing via the subduction of hydrous minerals. However, the overall balance of these fluxes at geological timescales remains uncertain. Geological observations suggest the stability of the long-term sea level and thus a near-steady-state regassing–degassing balance. In contrast, according to current thermopetrological modelling, the global input of H_2O inferred from geophysical observations leads to an unequivocal excess of regassing relative to degassing. Here we use recent experimental high-pressure data on natural hydrated peridotites to update the thermopetrological models and to reassess the calculations of H_2O fluxes into the mantle via subduction. Our models of 56 subduction transects show that a global input of $15-20 \times 10^8 \, TgH_2O$ every million years yields a limited global mantle regassing of $2.0-3.5 \times 10^8 \, TgH_2O$ every million years. The regassing occurs exclusively via the hydrated lithospheric mantle of the coldest subducting plates. Our requantification of the H_2O budget associated with subduction matches the estimations of mantle degassing and suggests that global sea levels have been relatively stable over geological timescales.

The water exchange between the Earth's surface and the deep interior is crucial for the evolution of our planet. Hydrous components affect the mantle rheology[1] and allow Earth-like plate tectonics[2], whereas liquid surface water is essential for planet habitability[3]. The mantle degasses H_2O through volcanism. Mantle regassing occurs via the subduction of H_2O chemically bound to hydrous minerals. However, metamorphic reactions with increasing temperature (T) and pressure (P) partly liberate this H_2O from the subducting oceanic plates. The fraction of the H_2O that is retained in the slab returns to the deep mantle, but its proportion remains debated. At first order, the imbalance between mantle degassing and regassing exerts a first-order control on the long-term eustatic sea level[4]. Hence, a precise quantification of the subducted H_2O fluxes is required to decipher the global water cycle.

The most comprehensive study of H_2O fluxes at present-day subduction zones[5] estimated a global water retention (GWR) of $3.4 \times 10^8 \, Tg \, Myr^{-1}$ beyond a 230 km depth. Their thermopetrological models predicted that half of the retention was controlled by the mafic crust, and a third by the hydrated lithospheric mantle, assumed to be only 2 km thick worldwide at subduction zone trenches. As mantle degassing is approximately $2 \times 10^8 \, Tg \, Myr^{-1}$ (refs. [6,7]), the predicted GWR would have decreased the global mean sea level by approximately 100 m over the Phanerozoic[6] (past 540 Myr, if constant over time). This is, however, close to the upper bound of retention that ensures a modest sea-level decrease (<100 m) during this eon, as inferred from stratigraphic constraints[6,8–10] (Extended Data Fig. 1).

Furthermore, reconstructions of time-dependent subduction rates in the Phanerozoic suggest that GWR was higher during specific events, for example, during the rift pulse at approximately 150 million years ago (Ma) (ref. [11]). A GWR at the present day of $3.4 \times 10^8 \, Tg \, Myr^{-1}$ or higher, as predicted by current thermopetrological models[5,12–14], seems thus inconsistent with a time-integrated low imbalance between mantle degassing and regassing. Only studies that neglected H_2O transfer via the hydrated mantle were able to reach such a criterion[15]. The growing evidence of a hydrated

lithospheric mantle thicker than 2 km (refs. [16–19]; see also Supplementary Section 3) and the potential ability of metasomatized ultramafic rocks at the slab–mantle interface to convey H_2O to the mid-mantle[20] urge the need to address this paradox.

The mineralogical changes in the subducting mafic crust and ultramafic mantle control the deep H_2O fluxes. Hence, quantitative studies of GWR rely on state-of-the-art petrological modeling of subducted hydrated lithologies.

Lawsonite is the main H_2O carrier in the crust beyond subarc depths (Fig. 1a). Its stability field is relatively well known from experimental studies[21,22]. In contrast, the postarc main hydrous phases for ultramafic systems are far less constrained[23,24]. The large uncertainties partly arise from the difficulty in handling laboratory H_2O-rich experiments with natural samples at the mid- to upper-mantle depth conditions. This is evidenced by the lack of experimental data on hydrous peridotite in the 6–8 GPa range (Supplementary Fig. 2b). Moreover, the poorly constrained effect of some minor elements (such as Al) and the unknown prevailing oxidation state of ultramafic rocks under high P and T conditions[24,25] preclude a proper petrological thermodynamic modelling of subducted ultramafic rocks. Consequently, experimental and modelled phase diagrams differ at pressures above 6 GPa (Fig. 1b,c and Supplementary Fig. 2a,b).

Here we improve the estimation of present-day GWR using recent experimental results on the stability of hydrous phases in natural hydrated peridotites. By considering the new experimental findings at high P and T conditions[24], the current view of relatively large amounts of H_2O reinjected into the deep upper mantle is challenged.

Thermopetrological models of present-day subduction zones

We modelled the thermal state of all present-day subduction zones (56 subduction transects[26]; Methods). We used the thermodynamic database of Holland and Powell[27] and the code Perple_X[28]

¹Géosciences Montpellier, University of Montpellier, CNRS, University of Antilles, Montpellier, France. ²Instituto Andaluz de Ciencias de la Tierra (IACT), CSIC–Universidad de Granada, Granada, Spain. ✉e-mail: nestor.cerpa@umontpellier.fr
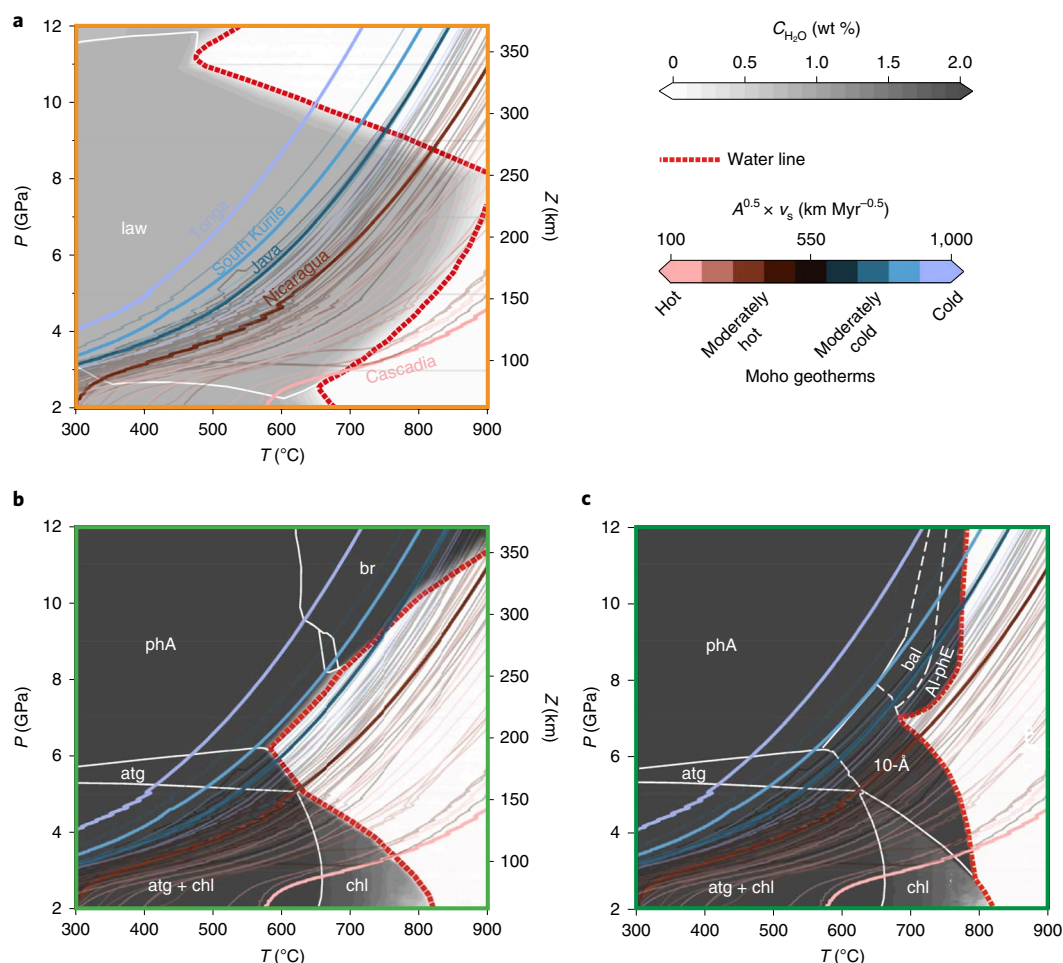
Fig. 1 | Geotherms at the Moho of the 56 modelled subduction transects plotted on top of diagrams of bound H$_2$O (C_{H_2O}). a–c, The diagrams are those for a gabbro (**a**), a thermodynamic peridotite model (**b**) and an experimental peridotite model (**c**). The stability fields of the main hydrous phases are depicted by white lines. For $T < 600\,°C$, antigorite and phase A form at pressures lower and higher than 6 GPa, respectively, in both peridotite models[21,25]. Chlorite is stable at T and P higher than 600 °C and lower than 6 GPa, respectively. The geotherms are represented by the coloured lines (all after a posteriori addition of an adiabatic gradient of 0.5 °C km^{-1}; see Methods), among which five are highlighted using thicker lines. The colour code follows the model's thermal state given by the product of the normal convergence rate (v_s) and the square root of the incoming plate age at the trench (A)[50]. law, lawsonite; atg, antigorite; chl, chlorite; phA, phase A; br, brucite; 10-Å, 10-Å phase; bal, balangeroite; Al-phE, aluminous phase E.

to build phase diagrams, assuming bulk compositions relevant for the crustal and mantle layers at the subduction trenches ('basalt' (Supplementary Fig. 5a), 'gabbro' and 'thermodynamic peridotite model' (Fig. 1a,b, respectively)). To enhance the accuracy of the modelled mineralogical evolution of hydrated peridotites up to mid-mantle depths, we combined thermodynamic modelling to experimentally derived assemblages from natural chemically complex systems[24] and we built a composite-phase diagram ('experimental peridotite model' Fig. 1c and Methods).

At shallow depths, H$_2$O subduction in the crustal layers occurs via amphibole, and at subarc to postarc depths via lawsonite[29]. At the depth where the slab surface starts to drag the overlying mantle[30,31], lawsonite is destabilized (700–900 °C at 8 GPa, Fig. 1a) within the basaltic uppermost layers of the subducting plates. Below, the slower heating of the gabbroic layer enables lawsonite stability for most subduction transects up to ~8 GPa. At higher pressures, the stability of lawsonite is rather temperature independent. Thus, in all but the hottest subduction transects (for example, Cascadia), the oceanic crust crosses its 'water line'[32], that is, the last phase transition beyond which hydrous minerals are unstable, between depths of 250 and 310 km.

The two petrological models for peridotite display important differences. Below 7 GPa, the formation of the 10-Å phase[33–35] enlarges the temperature range of the stability of hydrous minerals at ~5-6 GPa in the experimental model. However, the most striking differences that impact H$_2$O subduction are in the mineral assemblages above 8 GPa. In the thermodynamic model, phase A breaks down at approximately 650 °C to form brucite, the stability of which increases with pressure. In contrast, in the experimental model, brucite is absent. Balangeroite and aluminous phase E form instead[24], but within a narrower temperature range compared with that of brucite. These phase assemblages lead to notable differences in the water lines.

In the thermodynamically modelled system, the slope of the water line is negative below 6 GPa and positive above (Fig. 1b). The point of inflection (6 GPa and 580 °C), referred to as the 'choke point'[36], controls the H$_2$O retention in this system. The Moho geotherms (Tonga, South Kurile and Java) that pass above or near the choke point are quasi-parallel to the water line at higher P, which stabilizes hydrous minerals in the lithospheric mantle within a few kilometres below the Moho. The ability of a subducted mantle geotherm to pass the choke point has thus been related to its
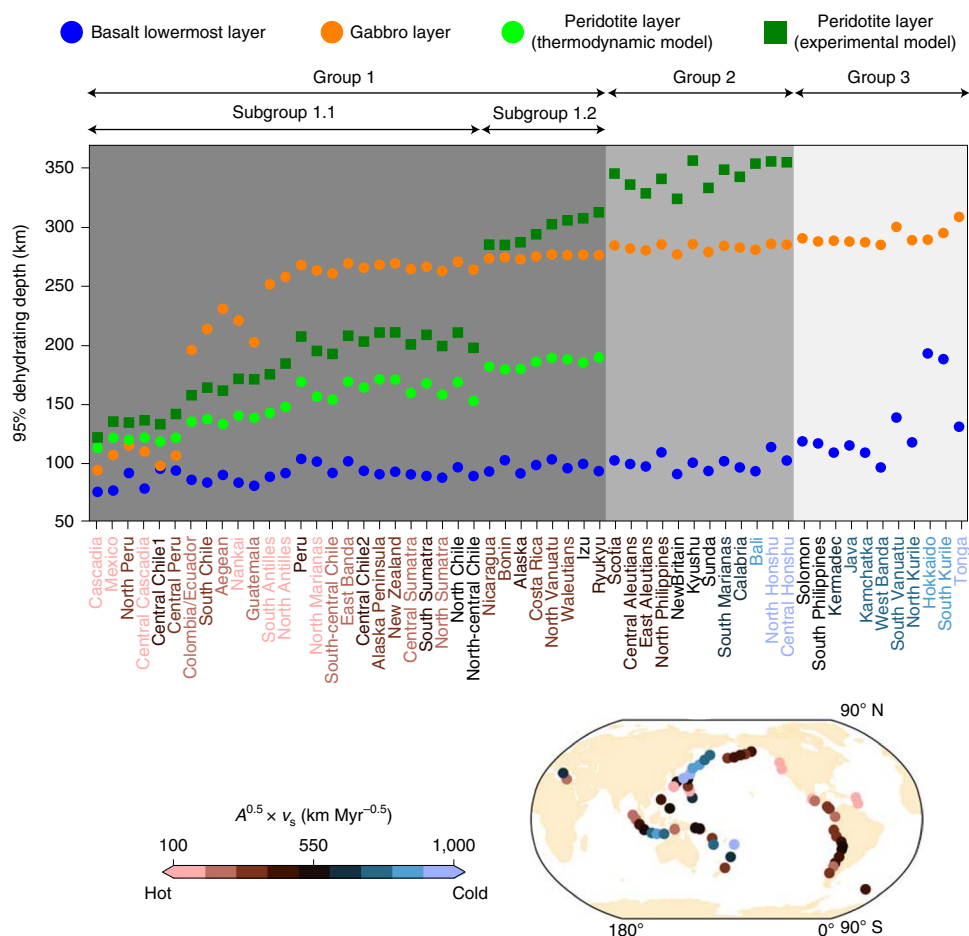
Fig. 2 | Depth of near-complete (95%) dehydration of the lithological layers for each subduction transect. The depth is that of the bottom of the layer when near-complete dehydration occurs. The absence of a symbol means that the layer has not reached 95% dehydration. Models with the two peridotite models are reported. Three groups are defined based on the dehydration mode of the hydrated mantle. Group 1: 95% dehydration of the mantle with all peridotite models; group 2: 95% dehydration before a 350 km depth only in models with the experimental peridotite model; group 3: 95% dehydration of the hydrated mantle not reached before a 350 km depth in any of the peridotite models.

capacity to carry H_2O down to mantle transition depths, at which very high P hydrous phases (E and D) may be stable over a wide range of temperatures[5,23,37].

In the experimental peridotite model, the choke point shifts to a higher T and P (680 °C and 7 GPa, Fig. 1c). This enlarges the range of Moho geotherms that stabilize hydrous minerals up to 6–7 GPa. However, as the phase transition from aluminous-phase E to nominally anhydrous peridotite is quasi-isothermal beyond 8 GPa (ref. [24]), many moderately cold Moho geotherms pass above the choke point but cross the water line between 9 and 12 GPa (for example, Java). The combined absence of brucite and the quasi-isothermal water line above 8 GPa thus become potential inhibitors of H_2O transport to great depths.

Near-complete dehydration depths

To illustrate the impact of the petrological assumptions, we calculated the depth at which the lowermost basaltic, the gabbroic and the hydrated peridotitic layers become nearly dry (95% dehydration; Methods). The latter is assumed to be 4 km thick (with a H_2O content of 2 wt%, that is, ~15% serpentinization) in our reference case, following previous studies of GWR[38].

The top basaltic layers are mainly dry near the depth at which the slab and mantle are kinematically coupled (that is, at 80–110 km). The dehydration of the gabbros occurs within the depth range of

200–300 km in all but the hottest subduction transects (Fig. 1a). The dehydration pattern of the lithospheric mantle is partly controlled by the thermal state of the transects, but primarily depends on the petrological model. We define three groups of transects based on the way the petrological assumptions impact the mantle dehydration pattern (Fig. 2).

Most transects belong to group 1, in which the lithospheric mantle dries within a depth range of 120–190 km, assuming the thermodynamic peridotite model. Considering the experimental peridotite model, the formation of the 10-Å phase in hot and moderately hot transects (subgroup 1.1) deepens the lithospheric mantle drying by 10 km (Cascadia) to 45 km (north central Chile). Apart from the hottest transects, the H_2O transport is limited by the breakdown of lawsonite in subgroup 1.1. If the 10-Å phase breaks down into balangeroite and aluminous-phase E (moderately cold geotherms, subgroup 1.2), dehydration occurs deeper than in the thermodynamic system and up to 310 km (Ryukyu) when the aluminous-phase E destabilizes. The transects in group 2 (moderately cold to cold geotherms) is not dry when a thermodynamic peridotite model is assumed, owing to the formation of phase A and brucite. In contrast, if the experimental peridotite model is assumed, the lithospheric mantle dries up between a 300 and 350 km depth, after the breakdown of aluminous-phase E. The hydrated mantle in the coldest slab transects, which form group 3, do not dry before
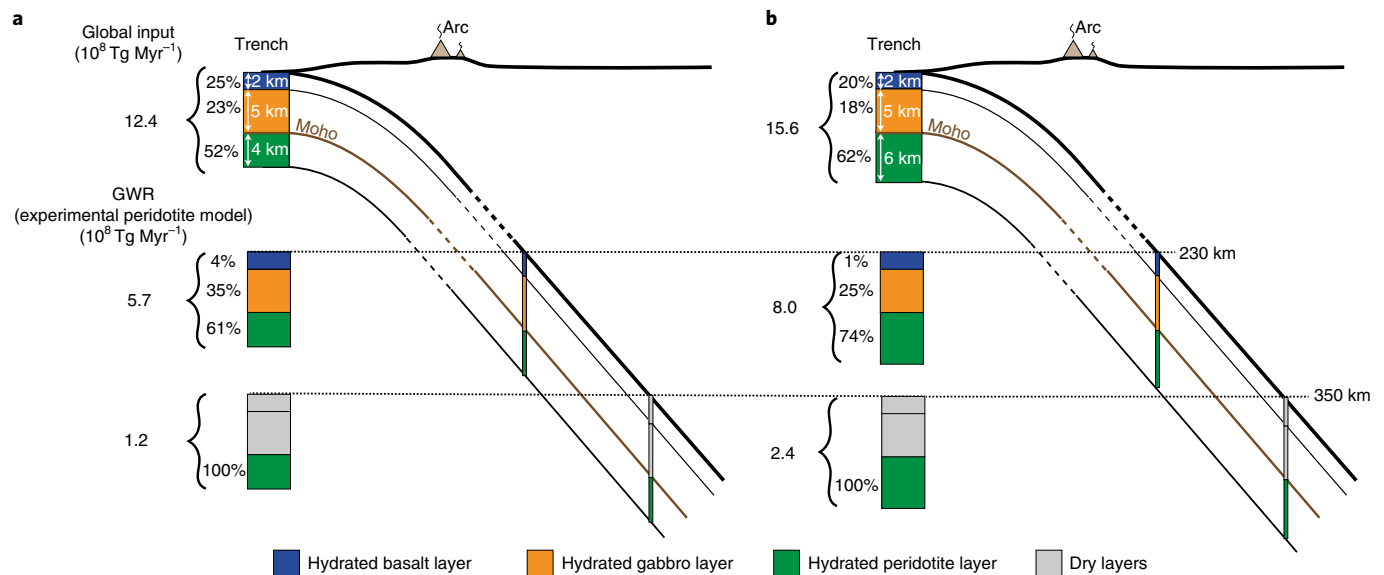
Fig. 3 | Global input of H₂O at the present-day subduction trenches and GWR computed using an experimental peridotite model. a,b, We display our reference model with a globally uniform thickness of hydrated mantle of 4 km (**a**) and of 6 km (**b**).

reaching the mid upper mantle regardless of the peridotite model. These coldest transects are the only ones able to convey H_2O to the mantle transition zone, according to our preferred experimental peridotite model.

Global water retention
We compared the global H_2O flux predictions to the bounds that allowed a relatively stable sea level during the Phanerozoic. The upper limit of $3.6 \pm 0.6 \times 10^8\,\mathrm{Tg\,Myr^{-1}}$ ensures a less than 100 m decrease of sea level[6] (Extended Data Fig. 1). The lower limit for GWR is derived from the total degassing of H_2O at mid-ocean ridges and ocean islands $(2.1 \pm 0.8 \times 10^8\,\mathrm{Tg\,Myr^{-1}}$ (ref. [7])), which would prevent an increase in sea level, consistent with the majority of reconstructions of eustatic sea level for the current eon[8,9] (although see Haq and Schutter[10]). Hence, we define the admissible GWR range as $2.1–3.6 \times 10^8\,\mathrm{Tg\,Myr^{-1}}$.

We first estimated the H_2O fluxes using the experimental peridotite model and our reference case assuming a globally uniform 4-km-thick hydrated mantle (Fig. 3a). The predicted global input of H_2O at the trenches is $12.4 \times 10^8\,\mathrm{Tg\,Myr^{-1}}$, which is consistent with previous estimations given the additional $10^8\,\mathrm{Tg\,Myr^{-1}}$ of H_2O input by sediments[5].

At a 230 km depth, that is, after mantle dehydration in subgroup 1.1, the GWR is $5.7 \times 10^8\,\mathrm{Tg\,Myr^{-1}}$ (Fig. 3a), driven by both the lithospheric mantle (61%) and the gabbroic layer (35%). Adding the potential H_2O flux subducted within the sediments[5] $(0.3 \times 10^8\,\mathrm{Tg\,Myr^{-1}})$, the resulting GWR at a depth of 230 km clearly overreaches the admissible GWR.

Gabbros (but also basalts and sediments) are all dry by a 300 km depth. Hence, the GWR at a 350 km depth is solely controlled by the lithospheric mantle of the coldest subduction zones (group 3) and equals $1.2 \times 10^8\,\mathrm{Tg\,Myr^{-1}}$ (65% of which results from retention in Tonga and South Vanuatu; Extended Data Fig. 2). Our modelled GWR is less than the admissible GWR. Note that slightly modified petrological assumptions (decreasing serpentinization with distance to the Moho and a reduced stability field of hydrous phases near the choke point; Supplementary Sections 4.4.3 and 4.4.5) have a subsidiary effect on the latter results. Assuming that the GWR was roughly stable through the Phanerozoic[5,6], the experimental peridotite

model predicts that mantle degassing slightly dominated. For comparison, use of the thermodynamic peridotite model nearly doubles the computed GWR at a 350 km depth (Fig. 4) and thus falls within the range of admissible GWR. However, as shown below, the latter observation does not hold when a more prominent hydration of the lithospheric mantle is considered, as proposed by multiple observations for natural subduction zones.

Extent of hydration at subduction trenches and GWR
Extensional earthquakes at the outer rise suggest that hydration mostly occurs within the first 5 km of the oceanic mantle[18]. Interestingly, the GWR computed assuming a globally uniform 6-km-thick hydrated mantle lies within the admissible GWR range only when the experimental peridotite model is considered (Figs. 3b and 4). Our prediction of GWR using a globally uniform 8-km-thick hydrated mantle exceeds this bound (Fig. 4 and Supplementary Section 4.4.1).

We nonetheless acknowledge that a globally uniform thickness of hydrated mantle might be a strong, and perhaps limiting, assumption. A compilation of the available data on the extent of mantle serpentinization at present-day subduction zones (thickness and serpentinization degree) shows, indeed, a worldwide disparity (Supplementary Section 3.1). We found that the serpentine content of the incoming plate correlates relatively well with a plastic radius of slab curvature[39]. This result was used to derive a parameterization of the mantle-hydrated thickness for each modelled transect (Supplementary Section 3.2).

The parameterized thickness of the hydrated mantle spans the range 0.8–8.8 km, with a global average of 5.6 km. The corresponding global input is similar to that computed with a globally uniform thickness of 6 km. As some of the cold subduction zones that promote deep H_2O retention are also predicted to host a thicker serpentinized mantle (Tonga and Kermadec), the GWR at a 350 km depth is higher $(3.1 \times 10^8\,\mathrm{Tg\,Myr^{-1}})$ than that in the uniform case with 6 km (Fig. 4). The GWR assuming a more realistic variable thickness of hydrated mantle nonetheless remains consistent with a modest sea-level decrease. We emphasize that both a worldwide variability in the extent of mantle hydration and the reduced stability field of hydrous phases predicted by the experimental petrological
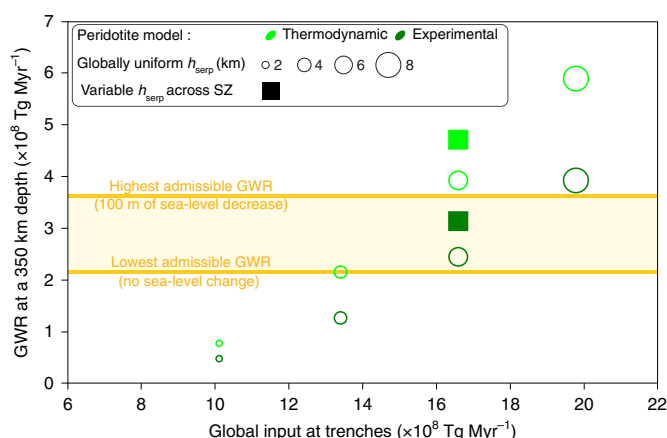
Fig. 4 | GWR at a 350 km depth as function of the global input at present-day subduction trenches. We display the estimations from various petrological assumptions, which include various thicknesses of hydrated mantle at the trenches. SZ, subduction zone. See Supplementary Information for how we calculated a variable h_{serp} across SZ.

model around the mid upper mantle P–T conditions ensures a modest return of H_2O to the deep upper mantle via only a few cold subduction zones.

Moreover, we note that the admissible-GWR constraint may be fulfilled only for a global input within the relatively narrow range of 16–19×10^8 Tg Myr^{-1}. It is also possible that a laterally heterogeneous hydration of the subducting plate along the trench outer rise faults induces a higher global input while preserving the compatibility with the admissible GWR. However, we still lack a global estimation database of such a lateral hydration at present-day subduction zones, which precludes an accurate modelling assessment of the related GWR (Supplementary Section 4.4.4).

Sensitivity of GWR to warmer conditions of subduction
The mantle temperature near the choke point of the thermodynamic peridotite model ($P \approx 6$ GPa) is crucial for the predictions of deep H_2O retention, as higher temperatures would lead to the mantle dehydration in the transects of groups 2 and 3. One could then hypothesize that an enhanced dehydration predicted with the thermodynamic peridotite model would reduce (or eliminate) the discrepancy between the computed and the admissible GWR. To test this, we performed additional models with warmer conditions of subduction: a high mantle potential temperature, a shallower coupling depth between the slab and the mantle, and shear heating along the subduction interface (Supplementary Section 5). Deeper than 150 km, this yields an increase in Moho temperatures of 35–70 °C at the choke-point pressure (6–7 GPa), depending on the transect, if the effective friction coefficient μ is equal to 0.03, and temperatures of 45–90 °C when μ is 0.05. Considering a global uniform serpentinized mantle thickness of 4 km, we found that warmer conditions with $\mu > 0.03$ and a thermodynamic peridotite model lead to a total amount of H_2O retained at a 350 km depth equivalent to that in the reference thermal conditions and the experimental peridotite model (Supplementary Fig. 14c). However, we note that to reach such an estimate the models need to be tuned to quite extreme warm conditions. We argue that these could hardly be reached in all subduction zones. Moreover, the warmer-condition assumption results in the release of the bound H_2O in the lithospheric mantle above depths of 200–250 km. It follows that such conditions would imply the quasi-absence of aqueous fluids available to assist the triggering of intermediate-to-deep seismicity observed beyond 200 km depth in many present-day subduction zones (see Supplementary

Section 6), which therefore also advocates for the relevance of the experimental peridotite model.

The fate of deep subducted H_2O
We estimate that the GWR at the mid upper mantle depths is 10–20% of the global input and that mantle regassing exceeds mantle degassing only in moderate proportions, as in our preferred model in which the local thicknesses of the hydrated mantle in the coldest subduction zones are as high as ~9 km. Hence, our novel thermopetrological models lessen the discrepancies between thermopetrological modelling of subductions zones, the geophysical evidence of large amounts of H_2O entering the trenches and the geological constraints on a long-term steady sea level.

An underlying assumption of our study is that all the H_2O release above a 350 km depth returns to the surface (that is, that mantle regassing is entirely controlled by the GWR). Other studies assumed, instead, that part of the released H_2O was conveyed by the downgoing mantle and contributed to mantle regassing[6]. We argue that compaction-driven porous flow may redirect most of the deep-released H_2O towards the arc[40,41], whether under the form of aqueous or supercritical fluids[42]. Some deep-released fluids may, nonetheless, be conveyed to the mantle transition zone through partitioning into nominally anhydrous minerals (~0.1 wt% (ref. [43])) but in moderate proportions compared with our estimated GWR.

Finally, our models may help explain other geophysical observations, such as the triggering of intermediate-to-deep seismicity. At the global scale, a drop in the number of volume-change-induced earthquakes in oceanic plates beyond mid upper mantle depths has been suggested to highlight that only a few dehydration reactions occur in the deep upper mantle[44–46]. Our first-order analysis of global seismicity reveals, in fact, that the subduction zones of groups 2 and 3 may host a moderate seismic activity within the depth range 200–350 km, and a weak activity beyond (Supplementary Figs. 6–15). If the triggering of these earthquakes is favoured by dehydrating-slab fluids, we stress that only the dehydration profiles from the experimental peridotite model could explain the vertical distribution of seismicity, especially at depths greater than 250 km. Our study also shows that the lithospheric mantle of the coldest slabs (for example, Tonga, Kermadec or Vanuatu) are the sole H_2O carriers beyond mid upper mantle depths. This may explain why, despite the potential ability of the mantle transition zone to be an important H_2O reservoir[47,48], global seismic surveys only show a heterogeneous hydration of the transition zone[49].

Online content
Any methods, additional references, Nature Research reporting summaries, source data, extended data, supplementary information, acknowledgements, peer review information; details of author contributions and competing interests; and statements of data and code availability are available at https://doi.org/10.1038/s41561-022-00924-3.

References
1. Hirth, G. & Kohlstedt, D. Rheology of the upper mantle and the mantle wedge: a view from the experimentalists. *Geophys. Monogr.* **138**, 83–106 (2003).
2. Regenauer-Lieb, K., Yuen, D. A. & Branlund, J. The initiation of subduction: criticality by addition of water? *Science* **294**, 578–580 (2001).
3. Kasting, J. F. & Catling, D. Evolution of a habitable planet. *Annu. Rev. Astron. Astrophys.* **41**, 429–463 (2003).
4. Conrad, C. P. The solid Earth's influence on sea level. *Bulletin* **125**, 1027–1052 (2013).
5. van Keken, P. E., Hacker, B. R., Syracuse, E. M. & Abers G. A, Subduction factory: 4. Depth-dependent flux of H_2O from subducting slabs worldwide. *J. Geophys. Res. Solid Earth* https://doi.org/10.1029/2010JB007922 (2011).

6. Parai, R. I. T. A. & Mukhopadhyay, S. U. J. O. Y. How large is the subducted water flux? New constraints on mantle regassing rates. *Earth Planet. Sci. Lett.* **317**, 396–406 (2012).
7. Hirschmann, M. M. Comparative deep Earth volatile cycles: the case for C recycling from exosphere/mantle fractionation of major (H_2O, C, N) volatiles and from H_2O/Ce, CO_2/Ba, and CO_2/Nb exosphere ratios. *Earth Planet. Sci. Lett.* **502**, 262–273 (2018).
8. Vail, P. R., Mitchum R. M. Jr & Thompson, S. III in *Seismic Stratigraphy— Applications to Hydrocarbon Exploration* (ed. Payton, C. E.) 83–98 (American Association of Petroleum Geologists Memoir 26, 1977).
9. Hallam, A. *Phanerozoic Sea-Level Changes* (Columbia Univ. Press, 1992).
10. Haq, B. U. & Schutter, S. R. A chronology of Paleozoic sea-level changes. *Science* **322**, 64–68 (2008).
11. Karlsen, K. S., Conrad, C. P. & Magni, V. Deep water cycling and sea level change since the breakup of Pangea. *Geochem. Geophys. Geosyst.* **20**, 2919–2935 (2019).
12. Rüpke, L. H., Morgan, J. P., Hort, M. & Connolly, J. A. Serpentine and the subduction zone water cycle. *Earth Planet. Sci. Lett.* **223**, 17–34 (2004).
13. Faccenda, M., Gerya, T. V. & Burlini, L. Deep slab hydration induced by bending-related variations in tectonic pressure. *Nat. Geosci.* **2**, 790–793 (2009).
14. Magni, V., Bouilhol, P. & van Hunen, J. Deep water recycling through time. *Geochem. Geophys. Geosyst.* **15**, 4203–4216 (2014).
15. Wallace, P. J. Volatiles in subduction zone magmas: concentrations and fluxes based on melt inclusion and volcanic gas data. *J. Volcanol. Geotherm. Res.* **140**, 217–240 (2005).
16. Ranero, C. R., Morgan, J. P., McIntosh, K. & Reichert, C. Bending-related faulting and mantle serpentinization at the Middle America trench. *Nature* **425**, 367–373 (2003).
17. Contreras-Reyes, E., Grevemeyer, I., Flueh, E. R. & Reichert, C. Upper lithospheric structure of the subduction zone offshore of southern Arauco peninsula, Chile, at ~38 °S. *J. Geophys. Res. Solid Earth* https://doi.org/10.1029/2007JB005569 (2008).
18. Emry, E. L. & Wiens, D. A. Incoming plate faulting in the Northern and Western Pacific and implications for subduction zone water budgets. *Earth Planet. Sci. Lett.* **414**, 176–186 (2015).
19. Cai, C., Wiens, D. A., Shen, W. & Eimer, M. Water input into the Mariana subduction zone estimated from ocean-bottom seismic data. *Nature* **563**, 389–392 (2018).
20. Hermann, J. & Lakey, S. Water transfer to the deep mantle through hydrous, Al-rich silicates in subduction zones. *Geology* https://doi.org/10.1130/G48658.1 (2021).
21. Schmidt, M. W. & Poli, S. Experimentally based water budgets for dehydrating slabs and consequences for arc magma generation. *Earth Planet. Sci. Lett.* **163**, 361–379 (1998).
22. Okamoto, K. & Maruyama, S. The high-pressure synthesis of lawsonite in the $MORB + H_2O$ system. *Am. Mineral.* **84**, 362–373 (1999).
23. Iwamori, H. Phase relations of peridotites under H_2O-saturated conditions and ability of subducting plates for transportation of H_2O. *Earth Planet. Sci. Lett.* **227**, 57–71 (2004).
24. Maurice, J. et al. The stability of hydrous phases beyond antigorite breakdown for a magnetite-bearing natural serpentinite between 6.5 and 11 GPa. *Contrib. Mineral. Petrol.* **173**, 86 (2018).
25. Maurice, J. et al. The intrinsic nature of antigorite breakdown at 3 GPa: experimental constraints on redox conditions of serpentinite dehydration in subduction zones. *Contrib. Mineral. Petrol.* **175**, 94 (2020).
26. Syracuse, E. M., van Keken, P. E. & Abers, G. A. The global range of subduction zone thermal models. *Phys. Earth Planet. Inter.* **183**, 73–90 (2010).
27. Holland, T. J. B. & Powell, R. An improved and extended internally consistent thermodynamic dataset for phases of petrological interest, involving a new equation of state for solids. *J. Metamorphic Geol.* **29**, 333–383 (2011).
28. Connolly, J. A. D. The geodynamic equation of state: what and how. *Geochem. Geophys. Geosyst.* https://doi.org/10.1029/2009GC002540 (2009).
29. Schmidt, M. & Poli, S. in *Treatise on Geochemistry* 2nd edn (eds Holland, H. D. & Turekian, K. K.) 669–701 (Elsevier, 2014).
30. Wada, I. & Wang, K. Common depth of slab-mantle decoupling: reconciling diversity and uniformity of subduction zones. *Geochem. Geophys. Geosyst.* https://doi.org/10.1029/2009GC002570 (2009).
31. Arcay, D. Dynamics of interplate domain in subduction zones: influence of rheological parameters and subducting plate age. *Solid Earth* **3**, 467–488 (2012).
32. Liu, L. G. Effects of H_2O on the phase behaviour of the forsterite–enstatite system at high pressures and temperatures and implications for the Earth. *Phys. Earth Planet. Inter.* **49**, 142–167 (1987).
33. Ulmer, P. & Trommsdorff, V. Serpentine stability to mantle depths and subduction-related magmatism. *Science* **268**, 858–861 (1995).
34. Fumagalli, P. & Poli, S. Experimentally determined phase relations in hydrous peridotites to 6.5 GPa and their consequences on the dynamics of subduction zones. *J. Petrol.* **46**, 555–578 (2005).
35. Dvir, O., Pettke, T., Fumagalli, P. & Kessel, R. Fluids in the peridotite–water system up to 6 GPa and 800 °C: new experimental constrains on dehydration reactions. *Contrib. Mineral. Petrol.* **161**, 829–844 (2011).
36. Kawamoto, T., Hervig, R. L. & Holloway, J. R. Experimental evidence for a hydrous transition zone in the early Earth's mantle. *Earth Planet. Sci. Lett.* **142**, 587–592 (1996).
37. Komabayashi, T. & Omori, S. Internally consistent thermodynamic data set for dense hydrous magnesium silicates up to 35 GPa, 1600 °C: implications for water circulation in the Earth's deep mantle. *Phys. Earth Planet. Inter.* **156**, 89–107 (2006).
38. Hacker, B. R. H_2O subduction beyond arcs. *Geochem. Geophys. Geosyst.* https://doi.org/10.1029/2007GC001707 (2008).
39. Buffett, B. A. & Heuret, A. Curvature of subducted lithosphere from earthquake locations in the Wadati–Benioff zone. *Geochem. Geophys. Geosyst.* https://doi.org/10.1029/2011GC003570 (2011).
40. Wilson, C. R., Spiegelman, M., van Keken, P. E. & Hacker, B. R. Fluid flow in subduction zones: the role of solid rheology and compaction pressure. *Earth Planet. Sci. Lett.* **401**, 261–274 (2014).
41. Cerpa, N. G., Wada, I. & Wilson, C. R. Fluid migration in the mantle wedge: influence of mineral grain size and mantle compaction. *J. Geophys. Res. Solid Earth* **122**, 6247–6268 (2017).
42. Mibe, K. et al. Second critical endpoint in the peridotite–H_2O system. *J. Geophys. Res. Solid Earth* https://doi.org/10.1029/2005JB004125 (2007).
43. Padrón-Navarta, J. A. & Hermann, J. A subsolidus olivine water solubility equation for the Earth's upper mantle. *J. Geophys. Res. Solid Earth* **122**, 9862–9880 (2017).
44. Omori, S., Komabayashi, T. & Maruyama, S. Dehydration and earthquakes in the subducting slab: empirical link in intermediate and deep seismic zones. *Phys. Earth Planet. Inter.* **146**, 297–311 (2004).
45. Green, H. W. II, Chen, W. P. & Brudzinski, M. R. Seismic evidence of negligible water carried below 400-km depth in subducting lithosphere. *Nature* **467**, 828–831 (2010).
46. Ferrand, T. P. Seismicity and mineral destabilizations in the subducting mantle up to 6 GPa, 200 km depth. *Lithos* **334**, 205–230 (2019).
47. Smyth, J. R. et al. Structural systematics of hydrous ringwoodite and water in Earth's interior. *Am. Mineral.* **88**, 1402–1407 (2003).
48. Fei, H. & Katsura, T. High water solubility of ringwoodite at mantle transition zone temperature. *Earth Planet. Sci. Lett.* **531**, 115987 (2020).
49. Houser, C. Global seismic data reveal little water in the mantle transition zone. *Earth Planet. Sci. Lett.* **448**, 94–101 (2016).
50. Maunder, B., van Hunen, J., Bouilhol, P. & Magni, V. Modeling slab temperature: a reevaluation of the thermal parameter. *Geochem. Geophys. Geosyst.* **20**, 673–687 (2019).

Methods

Thermal modelling. We considered two-dimensional thermomechanical models in which the kinematics of the subducting slab and of the overriding crust were prescribed but the creeping mantle wedge was dynamic. We solved the equations for mass and momentum conservation for an incompressible Boussinesq fluid:

$$\nabla \cdot \mathbf{v} = 0 \tag{1}$$

$$\nabla \cdot (2\eta \dot{\varepsilon}) - \nabla p = 0 \tag{2}$$

where $\mathbf{v}$ and p are the velocity and the dynamic pressure fields, respectively, ε is the strain-rate tensor and η is the shear viscosity. We considered a composite rheology (diffusion and dislocation) for the wedge in which the shear viscosity η is:

$$\frac{1}{\eta} = \left(\frac{1}{\eta_{\text{diff}}} + \frac{1}{\eta_{\text{disl}}} + \frac{1}{\eta_{\text{max}}} \right) \tag{3}$$

with η_{max} the maximum viscosity ($10^{24}\,\text{Pa}\,\text{s}$), and η_{diff} and η_{disl} the viscosities of diffusion and dislocation creep, respectively. They are given by:

$$\eta_i = \left(A_i b^{-\alpha_i} C_{\text{OH}}^{\beta_i} \exp\left(\frac{E_i}{RT}\right) \right)^{-\frac{1}{\gamma}} \dot{\varepsilon}_{\text{II}}^{\left(\frac{1-\gamma}{\gamma}\right)} \tag{4}$$

where the subscript i denotes either diffusion or dislocation creep, b is the grain size and ε_{II} is the second invariant of the strain rate. A, C_{OH}, E and R are the pre-exponential factor, water content, activation energy and gas constant, respectively. The parameters α, β and γ are the grain size, water content and stress exponents, respectively. The rheological parameters are set to experimentally determined values for wet olivine (Supplementary Table 2).

The energy conservation equation was solved under the assumption that the mantle flow has reached a steady state[41]:

$$\mathbf{v} \cdot \nabla T - \nabla \cdot (\kappa \nabla T) = Q \tag{5}$$

where T is the temperature field, κ is the thermal diffusivity and Q is a radiogenic heat source. The latter was assigned a low value of $0.02\,\mu\text{W}\,\text{m}^{-3}$, typical for the mantle. We did not include shear heating in the models, unless specified (Supplementary Section 5). For a few models, we included this source of heat along the plate interface down to the point at which the slab and the mantle wedge become coupled. This was done by adding to the right-hand side of equation (5) a term $Q_{\text{sh}} = \mu \sigma_{\text{n}} V$ where σ_{n} is the normal stress, μ is the effective friction coefficient and V is the downdip slab velocity.

The discretized problem with finite elements was solved with the software TerraFERMA[51]. We used an unstructured mesh with element sizes that ranged from approximately 1 km near the tip of the corner flow to 10 km sufficiently far from the tip for the gradients to be smoother.

Thermal model set-up. We performed tests for the 56 transects of major subduction zones defined in previous studies[5,26]. Our models consisted of a fixed rigid upper crust, a subducting slab with a prescribed velocity and a dynamic viscous mantle wedge that was coupled with the slab below a 75 km depth (Supplementary Fig. 1), except in the warmer-condition models in which we set this depth at 65 km (Supplementary Section 5). We adopted a realistic geometry for the top of the subducting slab based on the model Slab2.0[52]. For consistency, we considered realistic geometries above a 150 km depth. At higher depths, we extrapolated the slab surface with a constant dip to the bottom of the model domain. The imposed subducting slab velocity v_{sub} and upper crust thickness of each modelled transect are as in van Keken et al.[5] and Syracuse et al.[26]. The nature (continental versus oceanic), which defines the boundary condition on the back-arc side as discussed below, as well as the thickness of the upper plate, as well as the subduction velocity (trench, normal component) and slab age, are taken from Syracuse et al.[26]. The slab thermal structure at the trench is computed following the GDH1 plate cooling model[53]. At the bottom of the slab, we imposed the mantle potential temperature $T_{\text{m}} = 1{,}421.5\,^{\circ}\text{C}$ for consistency with the GDH1 plate cooling model, as in previous estimations of GWR[5]. Note that we also ran some models with $T_{\text{m}} = 1{,}450\,^{\circ}\text{C}$ (Supplementary Section 5). The surface temperature was set to $0\,^{\circ}\text{C}$. On the back-arc side, up to the mantle inflow–outflow transition depth, we imposed either the GDH1 model when the upper plate was oceanic or a one-dimensional conductive model if the upper plate was continental. The latter temperature boundary condition was capped to the mantle potential temperature. A free-stress boundary condition was imposed on the back-arc side.

Note that to map the modelled P–T conditions within the subducting slab onto the petrological phase relation grids described below, we added an a posteriori adiabatic gradient of $0.5\,^{\circ}\text{C}\,\text{km}^{-1}$ to the calculated temperature in the models.

Petrological modelling. We adopted a generic lithological model for the hydrated top of the oceanic plates entering the trench[38], which consisted of a 2-km-thick basaltic layer, a 5-km-thick gabbroic layer and a globally uniform thickness (h_{serp}) of the hydrated mantle, equal to 4 km in our reference case. We further considered cases with globally uniform thicknesses of the hydrated mantle equal to 2, 6 and

8 km, as well as a case in which h_{serp} varies as a function of the equivalent radius of curvature of the subduction transect (Supplementary Section 3). The basaltic layer was subdivided into a 0.3-km-thick upper volcanic layer, a 0.3-km-thick lower volcanic layer and a 1.4-km-thick dike layer, which differed by their initial H_2O contents of 3.1, 2.6 and 1.8 wt%, respectively. The gabbroic layer had an initial H_2O content of 0.8 wt%, and the hydrated lithospheric mantle an initial H_2O contents of 2 wt%, unless otherwise stated. Note that a H_2O content in the lithospheric mantle of 2 wt% corresponds to approximately 18% serpentinization, which is consistent with serpentinization degrees inferred from geophysical observations[38]. The phase relations were computed with the thermodynamic code Perple_X[28] using the thermodynamic database of Holland and Powell[27]. More details on the thermodynamic calculations are given in Supplementary Section 2.1. For the peridotite modelling, we refer to these computed phase relations as the thermodynamic peridotite model.

As the thermodynamic dataset for minerals and solid solutions that is used in common thermopetrological models has some important limitations (see below) for the investigated peridotite system, it must be understood that the current thermodynamic peridotite model carries these limitations. For instance, the most updated thermodynamic data set of Holland and Powell[27] does not include end members for the 10-Å phase, balangeroite or the Al-bearing phase E, that is, end members that form the solid solutions observed in experiments using natural (and therefore compositionally complex) serpentinite starting materials[24]. Moreover, there are no solid solution models that account for the effect of Al or Fe^{3+} on the 10-Å phase and phase E stability (but see Howe and Pawley[54]). Thus, to approximate the experimental peridotite model (that is, containing Al and Fe^{3+} in natural proportions), we combined the phase assemblages predicted by the low P and low T thermodynamic calculations with experimental data at high P and T for which the above ultra-high pressure phases have been experimentally observed[24,34,35], as explained below.

Experimental peridotite model. We first compiled the available experimental data on mineral phase assemblages using as the starting material either a natural serpentinite that contained ferric iron[24] or a hydrous synthetic lherzolite modelled in the complex chemical system Na_2O–CaO–FeO–MgO–Al_2O_3–SiO_2–H_2O (refs. [34,35]) at temperatures higher than $600\,^{\circ}\text{C}$ and pressures higher than 4 GPa (Supplementary Section 2.2 and Supplementary Fig. 2b). These reported phase relations serve as a basis for modifying the pseudosections obtained using Perple_X under these conditions (Supplementary Fig. 2a) and to build what we call a composite-phase diagram (Supplementary Fig. 2c). For simplicity, we refer to this petrological model as the experimental peridotite model because the low P and T predicted by the thermodynamic model used to construct the composite-phase diagram is in agreement with early experiments in this system. Given the lack of experimental data in the range 6.5–8 GPa, we derived two approximate phase transitions (the 10-Å phase to olivine and the Al-bearing phase E to olivine) at these P–T conditions for the composite-phase diagram: a high (HMmax) and a conservative (HMmin) estimate of the extent of the stability field of the hydrous phases (Supplementary Fig. 2c). Note that our calculations of GWR in the main text for the experimental peridotite model are based on the high estimate HMmax, as we observed little differences in the calculations with the low estimate (Supplementary Section 4.4.5). Mass balance calculations were performed to obtain the phase proportions in the composite-phase diagram for a fluid undersaturated peridotite composition, which allows us to infer the H_2O contents in the composite-phase diagram (Supplementary Fig. 2c).

Calculation of the H_2O fluxes. We adopted the approach of Wada et al.[55] to calculate the H_2O distribution in the two-dimensional subduction models. The hydrated portion of the subducting slab was divided into 500-m-wide vertical columns. The columns were further subdivided into cells with a height of 100 m. We then calculated the mass of H_2O retained by each cell given the P–T conditions at its centre. The temperature used for this calculation is that computed by the thermal models to which we add an a posteriori adiabatic gradient of $0.5\,^{\circ}\text{C}\,\text{km}^{-1}$. The total mass of the H_2O retained in each column (or lithological layer) is given by a summation of the H_2O content of the cells and converted into a mass flux ($\text{Tg}\,\text{Myr}^{-1}\,\text{m}^{-1}$) by using the horizontal projection of the subduction velocity at the top of the column. Note that, in our approach, the H_2O mass flux (water retention) at a given depth is that of the vertical column for which the top lies at this depth. We did not consider the rehydration of previously dehydrated cells[55]. We chose to compute the 95% dehydration depth instead of full dehydration to analyse the dehydration pattern of the hydrated lithologic layers (Fig. 2) for two reasons. First, in the mafic lithologies, phengite is stable up to 9.5 GPa and can retain residual amounts of H_2O (<0.2 wt%) after lawsonite breaks down. Thus, the depth of the total dehydration would not illustrate the condition at which most of the H_2O is released from the mafic lithologies. Second, our calculation of the H_2O content may also suffer from minor numerical artefacts that may lead to artificial residual amounts of H_2O retained in the computing cells, although the P–T conditions of dehydration were reached. Finally, to calculate the GWR, we multiplied the retention modelled for each transect by the corresponding length given by Syracuse et al.[26]. Note that the 4 wt% of GWR within the basaltic crust at a 230 km depth is due to both small amounts of actual H_2O retention by phengite and minor numerical artefacts.

Data availability
The numerical data generated for the 56 subduction transects (geotherms and water retention within the subducting slabs) are available in the Zenodo public repository https://doi.org/10.5281/zenodo.4632975.

Code availability
The code TerraFERMA used to compute the thermal models is open source and available at http://terraferma.github.io/. The thermodynamic code Perple_X is freely available at http://www.perplex.ethz.ch/ and information to reproduce the results is provided in Methods and the Supplementary Information.

References
51. Wilson, C. R., Spiegelman, M. & van Keken, P. E. Terra FERMA: The Transparent Finite Element Rapid Model Assembler for multiphysics problems in Earth sciences. *Geochem. Geophys. Geosyst.* **18**, 769–810 (2017).
52. Hayes, G. P. et al. Slab2, a comprehensive subduction zone geometry model. *Science* **362**, 58–61 (2018).
53. Stein, C. A. & Stein, S. A model for the global variation in oceanic depth and heat flow with lithospheric age. *Nature* **359**, 123–129 (1992).
54. Howe, H. & Pawley, A. R. The effect of solid solution on the stability of talc and 10-Å phase. *Contrib. Mineral. Petrol.* **174**, 81 (2019).
55. Wada, I., Behn, M. D. & Shaw, A. M. Effects of heterogeneous hydration in the incoming plate, slab rehydration, and mantle wedge hydration on slab-derived H_2O flux in subduction zones. *Earth Planet. Sci. Lett.* **353**, 60–71 (2012).
56. Crameri, F. Scientific colour-maps. *Zenodo* https://zenodo.org/record/2649252#.YjHEzainyUk (2018).

Author contributions
N.G.C. conceived the study, designed and performed the numerical models, analysed the results and wrote the first draft of the paper. D.A. provided funding for the project, participated in conceiving the study and analysed the results. J.A.P.-N. contributed to the petrological modelling and to the analysis of the results. All the authors discussed the implications of the study and wrote the manuscript.

Competing interests
The authors declare no competing interests.

Additional information
Extended data is available for this paper at https://doi.org/10.1038/s41561-022-00924-3.

Supplementary information The online version contains supplementary material available at https://doi.org/10.1038/s41561-022-00924-3.

Correspondence and requests for materials should be addressed to N. G. Cerpa.

Peer review information *Nature Geoscience* thanks Valentina Magni and the other, anonymous, reviewer(s) for their contribution to the peer review of this work. Primary Handling Editor: Rebecca Neely, in collaboration with the *Nature Geoscience* team.

Reprints and permissions information is available at www.nature.com/reprints.

Study	Mean sea level change over the last 542 Ma	Global Input [10^8 Tg/Myr]	GWR [10^8 Tg/Myr]
refs. 8,9,10	-75 m (average from ref. 6)		
ref. 7	0 m*		2.1*
ref. 6	0 m -100 m	10.8	2.5 3.6
ref. 5		10.0	3.4

Extended Data Fig. 1 | Previous estimates of mean sea level change in the Phanerozoic, global input and GWR. The first row displays the average change in sea level over the Phanerozoic derived from geological constraints. The second and third row provide bounds on the GWR (admissible GWR) compatible with a 0 to 100-m of change in sea-level. Note that the asterisk (2nd row) denotes an indirect bound where we have assumed that a 0-m change of sea level over the Phanerozoic will be achieved if the GWR is equal to the total H_2O degassing both at mid-ocean ridges and at ocean islands. The fourth row shows the estimated GWR by the thermopetrological models of ref. [5].
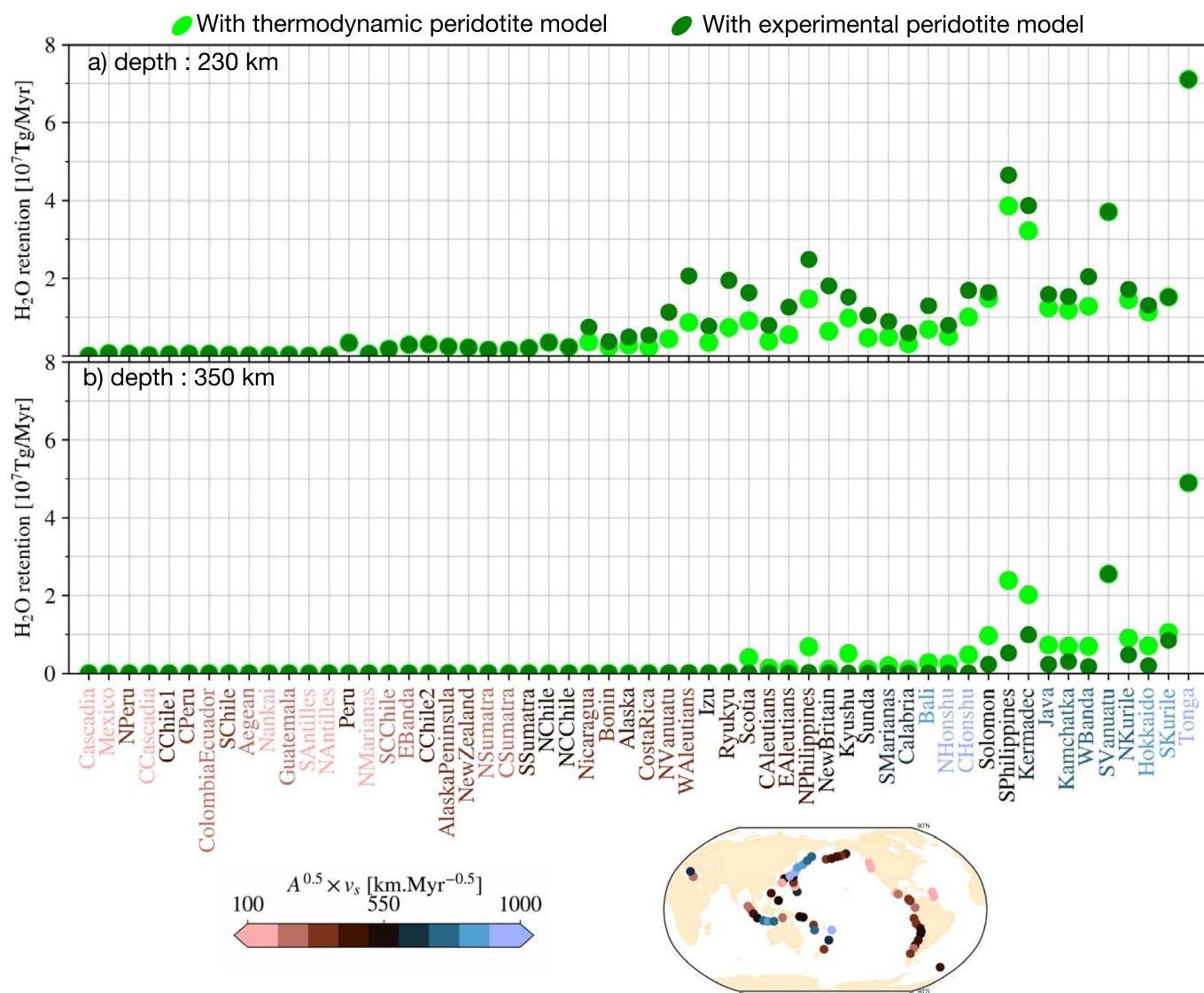
Extended Data Fig. 2 | H2O retention per subduction zone at depths of 230 km and 350 km assuming a globally-uniform thickness of 4 km for the hydrated mantle. H2O retention per subduction zone at depths of 230 km **(a)** and 350 km **(b)** assuming a globally-uniform thickness of 4 km for the hydrated mantle. The calculations with our two peridotite models are displayed. The names of the subduction zones are color-coded as a function of their thermal state (see Fig. 1).